Electronic Supplementary Information

Rational Design of $Na(Li_{1/3}Mn_{1/2}Cr_{1/6})O_2$ Exhibiting Cation-Anion-Coupled Redox Reactions with Superior Electrochemical, Thermodynamic, Atomic, and Chemomechanical Properties for Advanced Sodium-Ion Batteries

Duho Kim, Maenghyo Cho and Kyeongjae Cho**

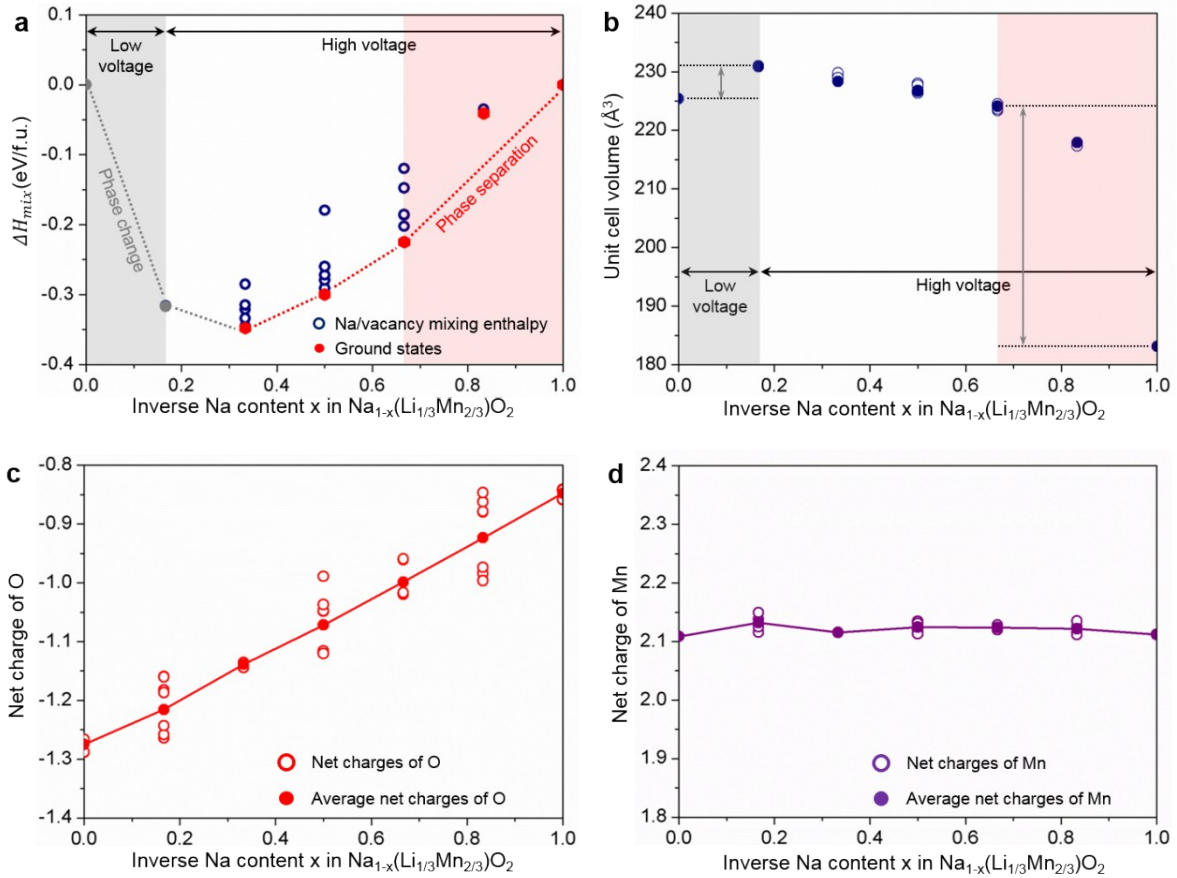

Fig. S1 Reaction mechanism of $Na(Li_{1/3}Mn_{2/3})O_2$. **a** Mixing enthalpy values considering all possible Na/vacancy configurations for $0 \leq x \leq 1.0$ in $Na_{1-x}(Li_{1/3}Mn_{2/3})O_2$. **b** Calculated unit cell volume and net charges for **c** O and **d** Mn as a function of the inverse Na content (x) in $Na_{1-x}(Li_{1/3}Mn_{2/3})O_2$. The mixing enthalpies and net charges are reproduced from a previous report by us.[1]

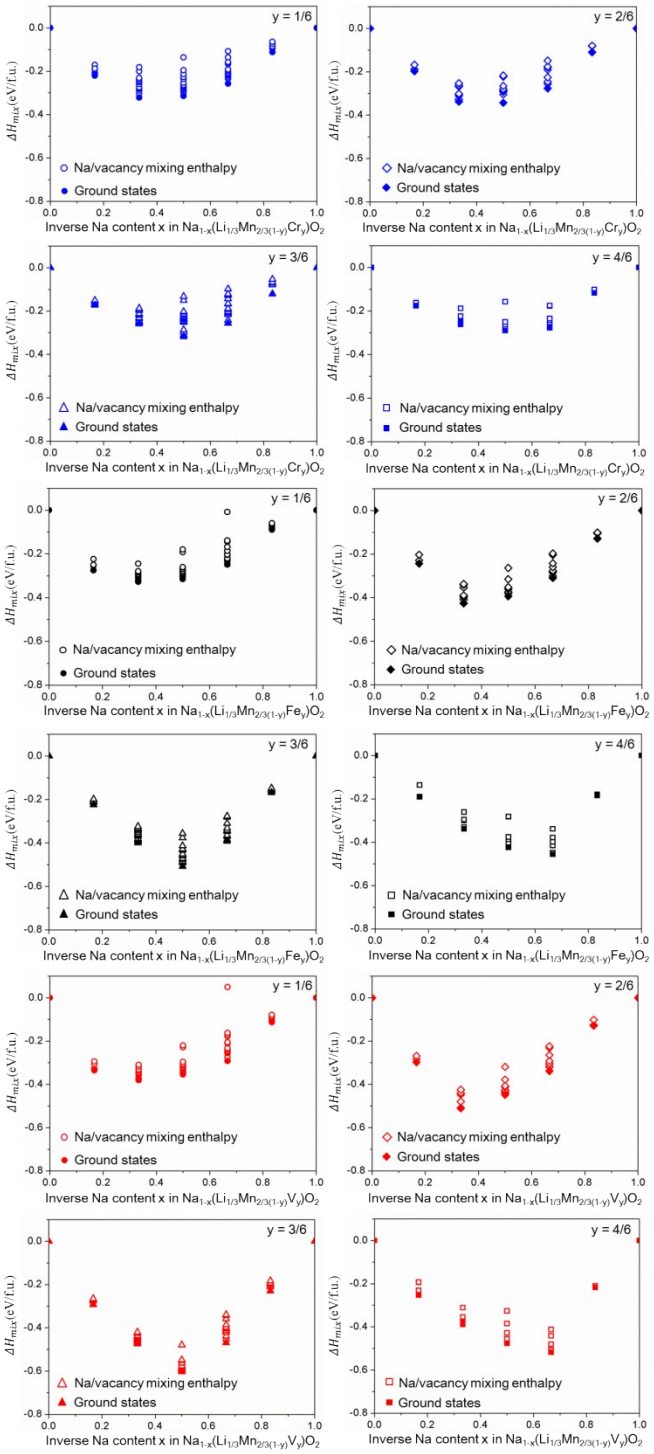

Fig. S2 Thermodynamic phase behaviors. Mixing enthalpy values considering all possible Na/vacancy configurations as a function of the inverse Na content (x) in $Na_{1-x}(Li_{1/3}Mn_{2/3(1-y)}M_y)O_2$ (M: Cr, Fe, and V) at varying y values (y = 1/6, 2/6, 3/6, and 4/6).

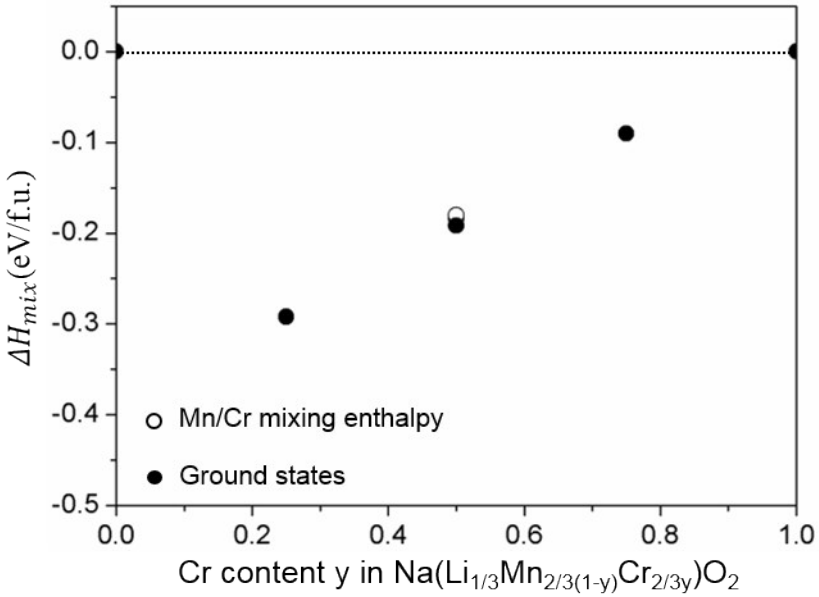

Fig. S3 Thermodynamic phase stability with varying Cr content. Mixing enthalpy values considering all possible Mn/Cr configurations as a function of the Cr content (*y*) in $Na(Li_{1/3}Mn_{2/3(1-y)}Cr_{2/3y})O_2$.

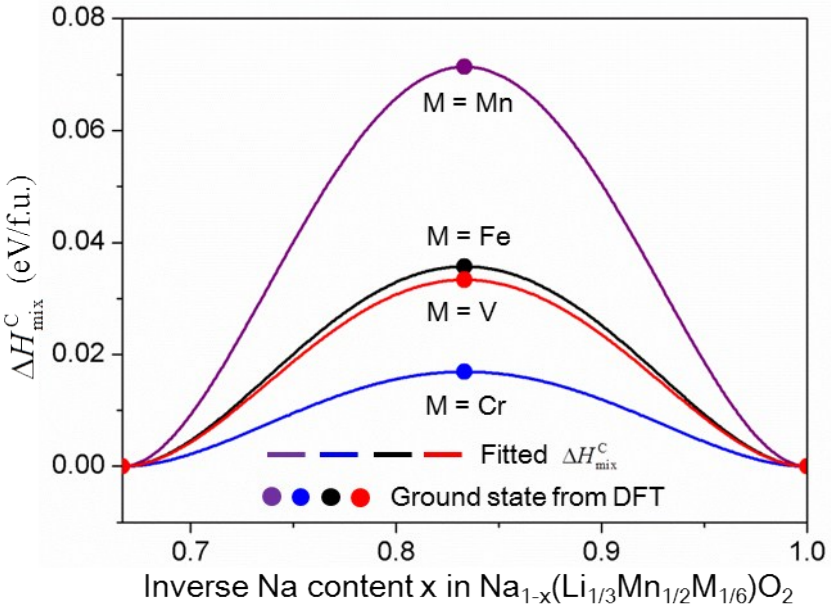

Fig. S4 Multiscale bridging model. Configurational homogeneous mixing enthalpies fitted from the mixing enthalpies at x = 4/6, 5/6, and 1.0 in $Na_{1-x}(Li_{1/3}Mn_{1/2}M_{1/6})O_2$ (M: Mn, Cr, Fe, and V) from Figs. 2b–e using a double-well function.

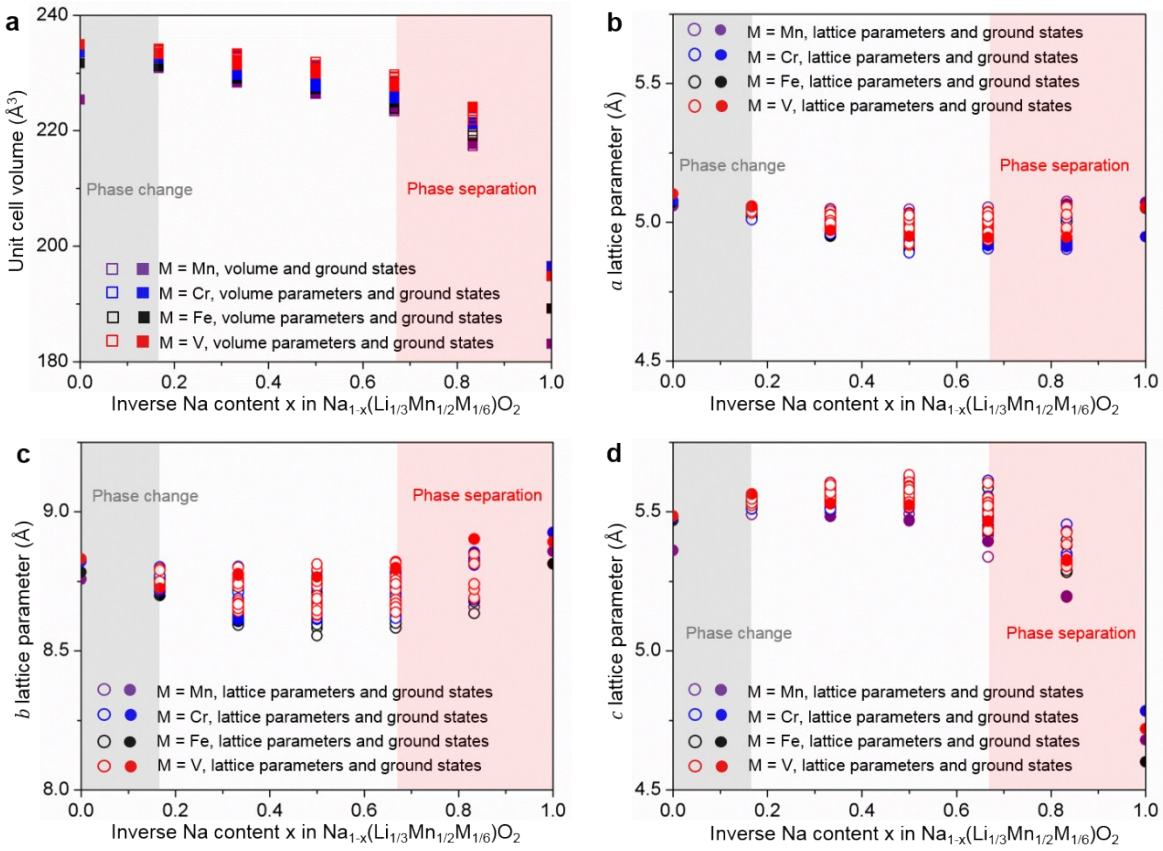

Fig. S5 Structural investigations during desodiation. Calculated structural parameters (**a** unit cell volume, and **b** *a*, **c** *b*, and **d** *c* lattice parameters) as a function of the inverse Na content (x) in $Na_{1-x}(Li_{1/3}\ Mn_{1/2}M_{1/6})O_2$ (M: Mn, Cr, Fe, and V).

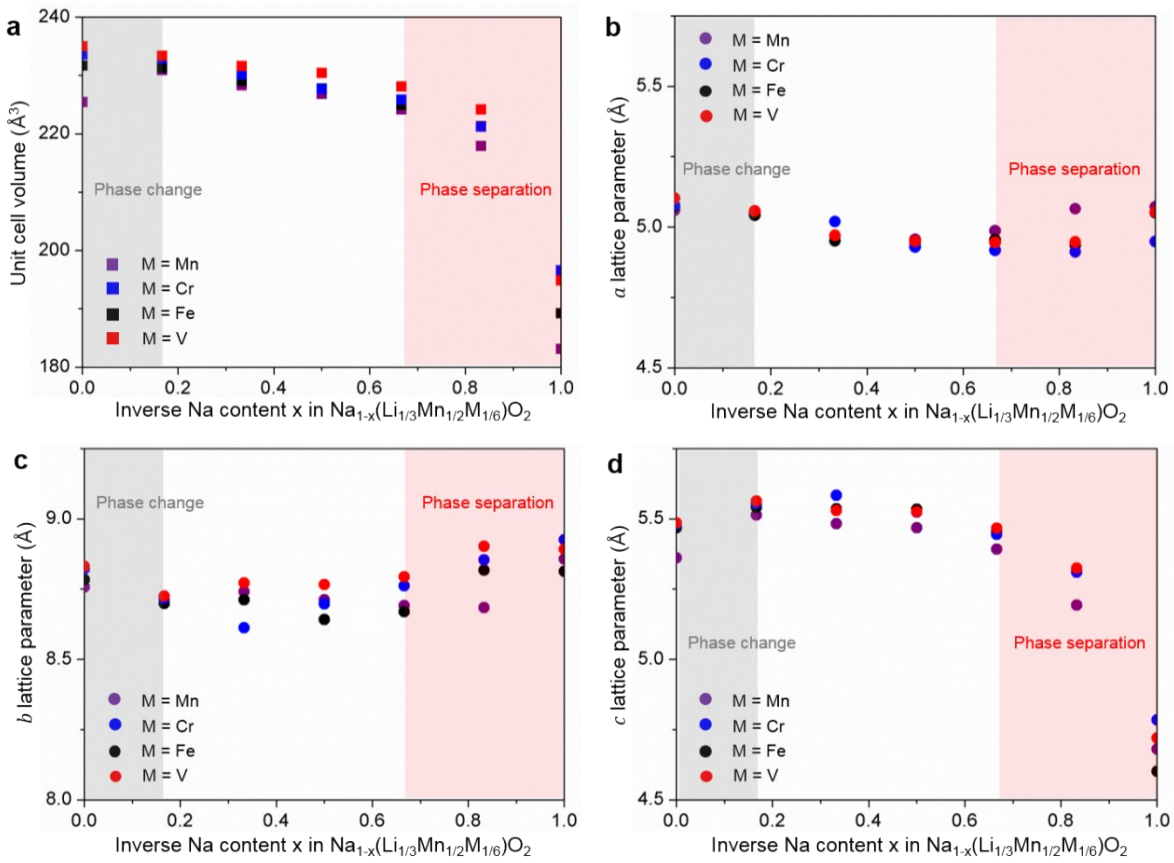

Fig. S6 Structural parameters at ground states during desodiation. Structural parameters for the ground states from Fig. S5 as a function of the inverse Na content (x) in $Na_{1-x}(Li_{1/3}Mn_{1/2}M_{1/6})O_2$ (M: Mn, Cr, Fe, and V).

Table S1 Thermodynamic formation energy considering structural changes. Structural formation energy of NLMO and NLMCO, illustrating the difference between the rigid body mode of the $Na_0(Li_{1/3}Mn_{2/3})O_2$ and $Na_0(Li_{1/3}Mn_{1/2}Cr_{1/6})O_2$ structures and the fully relaxed $Na_0(Li_{1/3}Mn_{2/3})O_2$ and $Na_0(Li_{1/3}Mn_{1/2}Cr_{1/6})O_2$ structures.

Compound	Structural formation energy (eV)
NLMO	-0.8715
NLMCO	-0.6126

Table S2 Elastic constants of C_{33} during desodiation. C_{33} elastic constant as a function of the inverse Na content in $Na_{1-x}(Li_{1/3}Mn_{2/3})O_2$ and $Na_{1-x}(Li_{1/3}Mn_{1/2}Cr_{1/6})O_2$. For better understanding, the elastic constants are plotted in Fig. S7.

Inverse Na content (x)	Elastic constant C_{33}	
	$Na_{1-x}(Li_{1/3}Mn_{2/3})O_2$	$Na_{1-x}(Li_{1/3}Mn_{1/2}Cr_{1/6})O_2$
0.0	244.5072	248.7740
0.1667	215.9338	238.7789
0.3333	193.2726	226.6244
0.5	165.4752	186.9789
0.6667	133.1598	159.4715
0.8333	103.3250	135.0344
1.0	332.7202	132.3336

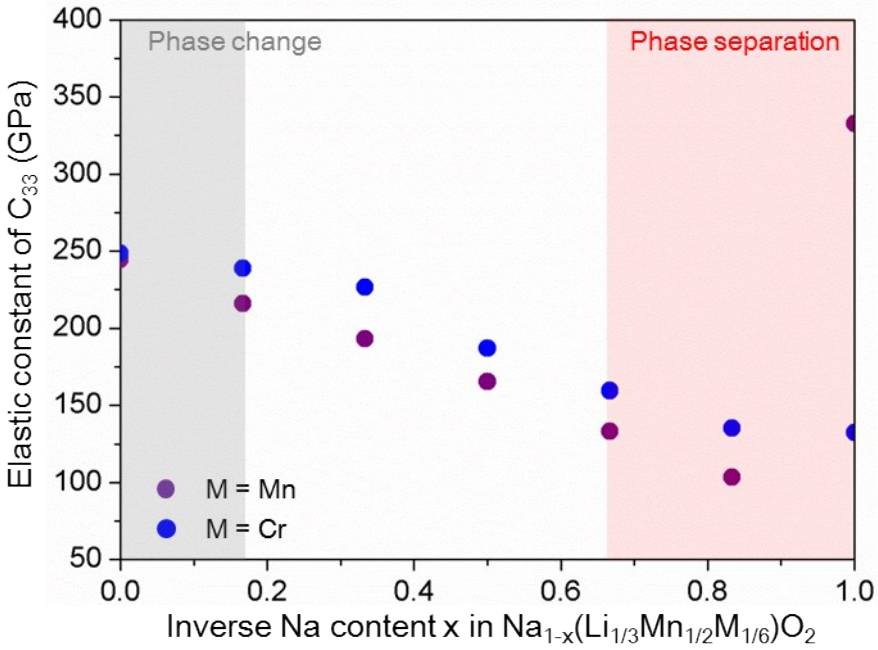

Fig. S7 Elastic constants of C_{33} during desodiation. C_{33} elastic constant, from Table S2, as a function of the inverse Na content (x) in $Na_{1-x}(Li_{1/3}Mn_{2/3})O_2$ and $Na_{1-x}(Li_{1/3}Mn_{1/2}Cr_{1/6})O_2$.

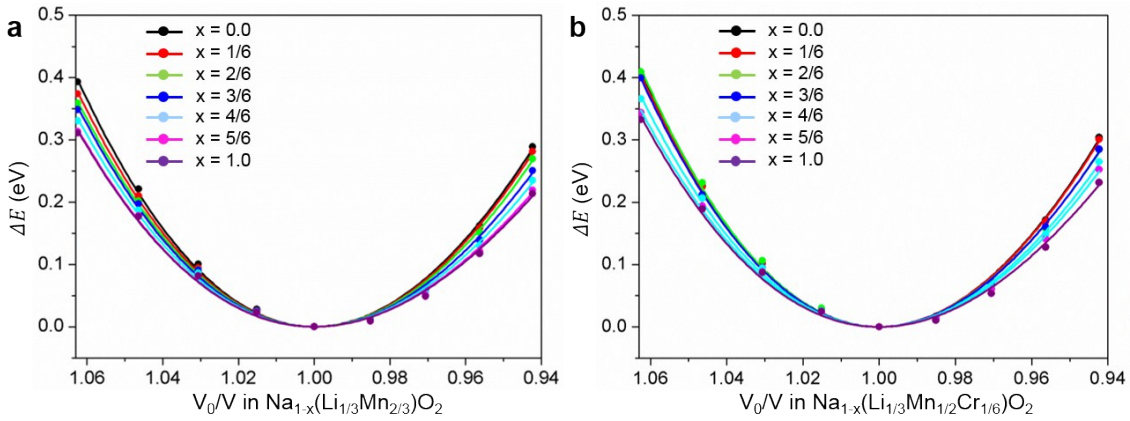

Fig. S8 Energy investigations varying volume changes. Changes in the strain energy (ΔE) as a function of the volume ratio (V_0/V) in $Na_{1-x}(Li_{1/3}Mn_{2/3})O_2$ and $Na_{1-x}(Li_{1/3}Mn_{1/2}Cr_{1/6})O_2$. The solid lines represent the fitted results using the Birch–Murnaghan equation of states, based on the total energies calculated by the first-principles method.

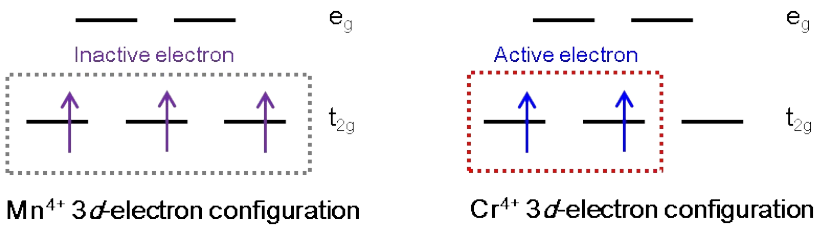

Fig. S9 Schematic energy band diagram based on crystal field theory. Schematic electronic configuration of Mn^{4+} (t_{2g}^3 e_g^0) and Cr^{4+} (t_{2g}^2 e_g^0) at the octahedral sites of the oxide based on crystal field theory. Compared to the stabilized Mn^{4+} electronic structure, the electronic configuration of Cr^{4+} is expected to be active for oxidation reactions, indicating a double redox behavior (Cr^{4+}/Cr^{6+}) upon Na extraction.

Table S3 Octahedral structure investigations during desodiation. Average octahedral volume (MnO_6 and CrO_6) and bond lengths (Mn–O and Cr–O) with respect to the inverse Na content (x) in $Na_{1-x}(Li_{1/3}Mn_{2/3})O_2$ and $Na_{1-x}(Li_{1/3}Mn_{2/3}Cr_{1/6})O_2$ ($0 \leq x \leq 1.0$). The octahedral volumes and bond lengths of MnO_6 and CrO_6 in $Na(Li_{1/3}Mn_{2/3}Cr_{1/6})O_2$ are larger than those in MnO_6 for $Na(Li_{1/3}Mn_{2/3})O_2$, which originate from the larger ionic radius of Cr^{4+} versus Mn^{4+}. The octahedral volume and bond lengths of CrO_6 drastically decrease up to $x = 0.3333$ in $Na_{1-x}(Li_{1/3}Mn_{2/3}Cr_{1/6})O_2$ compared to those of MnO_6 in $Na_{1-x}(Li_{1/3}Mn_{2/3})O_2$, reflecting the cationic redox reaction of the Cr 3d electrons (PDOS and net charges are shown in Fig. 4) in octahedral configuration. All the calculated results are plotted in Fig. S10.

Compounds: $Na_{1-x}(Li_{1/3}Mn_{2/3})O_2$ ($Na_{1-x}(Li_{1/3}Mn_{1/2}Cr_{1/6})O_2$)				
Inverse Na content	Average octahedral volume		Average bonding length (M–O)	
	MnO_6	CrO_6	MnO_6	CrO_6
0.0	9.4956 (9.7040)	(9.6975)	1.9316 (1.9448)	(1.946)
0.1667	9.5115 (9.5846)	(8.8533)	1.9316 (1.9373)	(1.8870)
0.3333	9.3319 (9.4005)	(8.2497)	1.9192 (1.9259)	(1.8425)
0.5	9.1857 (9.2685)	(8.1715)	1.9104 (1.9175)	(1.8380)
0.6667	9.0907 (9.2136)	(8.1259)	1.9063 (1.9177)	(1.8455)
0.8333	9.1088 (9.1804)	(8.0953)	1.9111 (1.9199)	(1.8507)
1.0	9.1230 (9.1701)	(7.9971)	1.9157 (1.9224)	(1.8434)

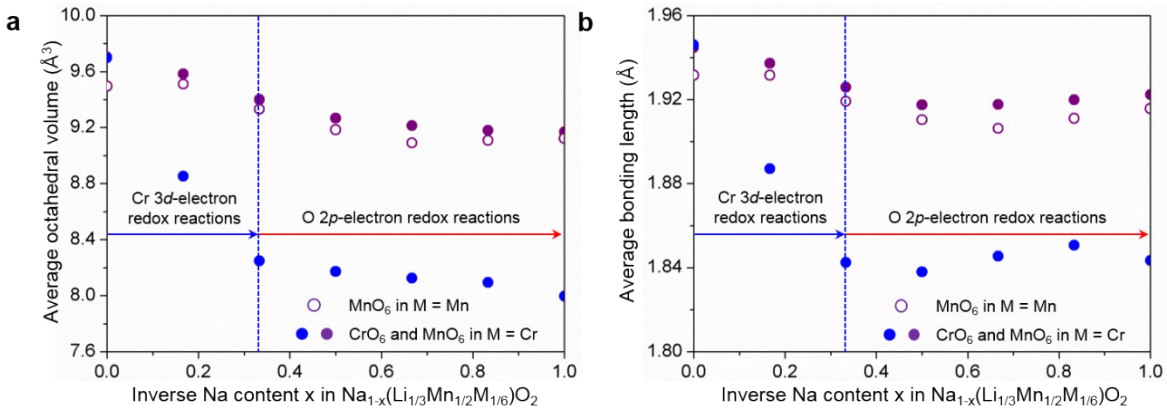

Fig. S10 Octahedral structure investigations during desodiation. a Average octahedral volume of MnO_6 in $Na_{1-x}(Li_{1/3}Mn_{2/3})O_2$ and those of MnO_6 and CrO_6 in $Na_{1-x}(Li_{1/3}Mn_{2/3}Cr_{1/6})O_2$ at varying x values ($0 \leq x \leq 1.0$). **b** Average Mn–O bond length in $Na_{1-x}(Li_{1/3}Mn_{2/3})O_2$, and those of Mn–O and Cr–O in $Na_{1-x}(Li_{1/3}Mn_{2/3}Cr_{1/6})O_2$ at varying x values ($0 \leq x \leq 1.0$).

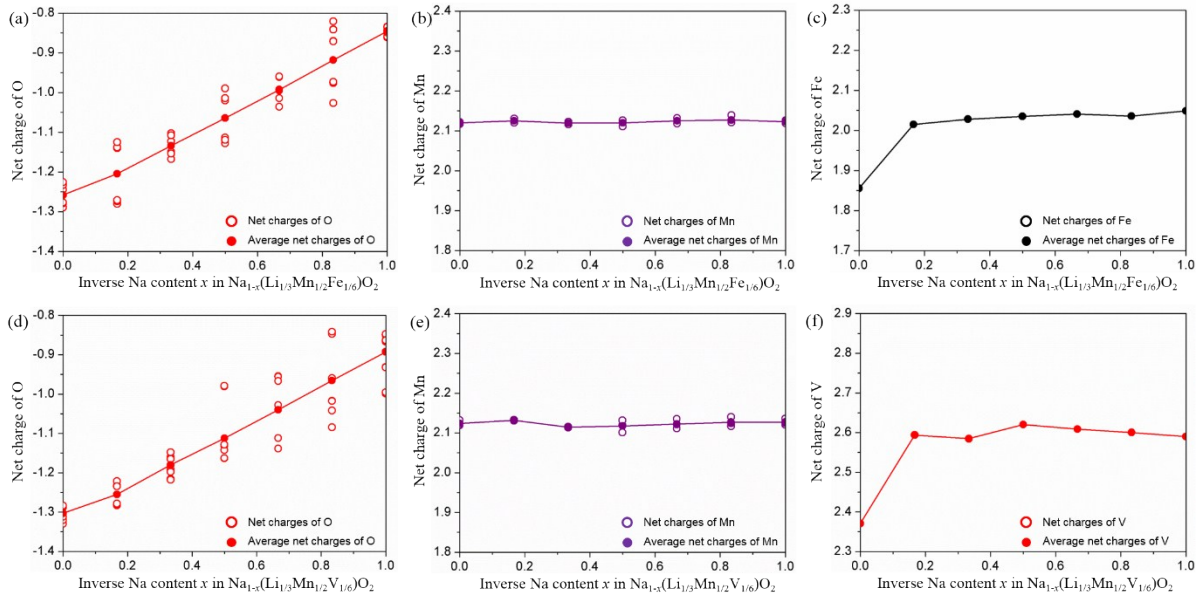

Fig. S11 Redox mechanism of NLMFO and NLMVO. Net charges calculated by the Bader charge method for **a** O, **b** Mn, and **c** Fe as a function of the inverse Na content (x) in $Na_{1-x}(Li_{1/3}Mn_{1/2}Fe_{1/6})O_2$. Those for **d** O, **e** Mn, and **f** V as a function of the inverse Na content (x) in $Na_{1-x}(Li_{1/3}Mn_{1/2}V_{1/6})O_2$. The net charges of Mn for both oxides do not change with respect to the inverse Na content, whereas those of Fe and V vary linearly up to x = ~1/6 for each oxide. Linear increases of the O net charges are observed over the full range ($0 \leq x \leq 1.0$). These charge behaviors identify the cation-anion-coupled redox mechanism as confirmed in NLMCO. From the perspective of thermodynamics, Figure 2d,e shows that the two intermediate phases as marked with black and red filled circles, lying above the tile lines (dotted lines) at x = 4/6 and at x = 1.0, at x = 5/6 are more stable for NLMFO and NLMVO than for NLMO because the two phases are more closer to the tie lines than that of NLMO. In a better understanding of phase behaviour, the homogeneous bulk free energies and homogeneous chemical potentials of NLMFO and NLMVO indicate lowered spinodal decomposition barriers and thermodynamic hysteresis gaps as compared with NLMO. From the structural viewpoint, Figure 4a shows that the volumetric strains of NLMFO and NLMVO are remarkably alleviated in comparison with NLMO. Similar to NLMCO, suppressed tensile volumetric strains are observed during the initial desodiaton and compressive volumetric

strains at a much slower rate take place in the phase separation region for NLMFO and NLMVO. These results suggest that Fe and V can be substituted for Cr.

References

1. D. Kim, M. Cho and K. Cho, *Adv Mater*, 2017, **29**.